

Coupled optical and electrical modeling of solar cell based on conical pore silicon photonic crystals

Alexei Deinega, Sergey Eyderman, and Sajeev John

Citation: *J. Appl. Phys.* **113**, 224501 (2013); doi: 10.1063/1.4809982

View online: <http://dx.doi.org/10.1063/1.4809982>

View Table of Contents: <http://jap.aip.org/resource/1/JAPIAU/v113/i22>

Published by the [American Institute of Physics](#).

Additional information on J. Appl. Phys.

Journal Homepage: <http://jap.aip.org/>

Journal Information: http://jap.aip.org/about/about_the_journal

Top downloads: http://jap.aip.org/features/most_downloaded

Information for Authors: <http://jap.aip.org/authors>

ADVERTISEMENT



AIP Advances

Now Indexed in Thomson Reuters Databases

Explore AIP's open access journal:

- Rapid publication
- Article-level metrics
- Post-publication rating and commenting

Coupled optical and electrical modeling of solar cell based on conical pore silicon photonic crystals

Alexei Deinega,^{a)} Sergey Eyderman, and Sajeev John

Department of Physics, University of Toronto, 60 St. George Street, Toronto, Ontario M5S 1A7, Canada

(Received 25 March 2013; accepted 27 May 2013; published online 10 June 2013)

We compare the efficiency of thin film photonic crystal solar cells consisting of conical pores and nanowires. Solving both Maxwell's equations and the semiconductor drift-diffusion in each geometry, we identify optimal junction and contact positions and study the influence of bulk and surface recombination losses on solar cell efficiency. We find that using only $1\ \mu\text{m}$ of silicon, sculpted in the form of an inverted slanted conical pore photonic crystal film, and using standard contact recombination velocities, solar power conversion efficiency of 17.5% is obtained when the carrier diffusion length exceeds $10\ \mu\text{m}$. Reducing the contact recombination velocity to $100\ \text{cm s}^{-1}$ yields efficiency up to 22.5%. Further efficiency improvements are possible (with $1\ \mu\text{m}$ of silicon) in a tandem cell with amorphous silicon at the top. © 2013 AIP Publishing LLC. [<http://dx.doi.org/10.1063/1.4809982>]

I. INTRODUCTION

Silicon is the most widely used material for solar cell production due to its abundance, nontoxicity, reliability, and mature fabrication process. At the present time, solar cells based on silicon occupy most of the photovoltaics market. Currently, the best efficiency of commercial silicon solar modules is around 17.5%.^{1–3} Silicon is an indirect-bandgap semiconductor which results in moderate absorption length. To absorb enough of the solar spectrum, the thickness of the silicon planar cell is typically more than $100\ \mu\text{m}$. In order to collect all generated carriers before they recombine, the carrier diffusion length in silicon should be comparable to the cell thickness. This requirement for a large volume of high quality silicon constitutes a significant part of silicon solar cell cost. Thin film technology is a promising way to avoid these cost issues. However, best thin film samples of thickness less than $10\ \mu\text{m}$ yield an efficiency of around 10%, which is low compared to wafer-based cells.^{4,5} This is due to poor light absorption in thin silicon films.

Some enhancement in solar absorption is achieved by texturing the surface of silicon thin films with nanocones or nanoholes. This provides an antireflective mechanism at the top surface of the cell for incident light. In the long wavelength regime, the texture acts like a graded index film with low reflection above the active region of the solar cell.^{6–11} In the short wavelength regime, suppression of the reflection occurs because rays must be reflected many times before being backscattered.^{12,13} In the visible range, textured surfaces with the periodicity of the optical wavelength are highly efficient.^{14–18} Recently, antireflective properties of textured surfaces in a whole range of size-to-wavelength ratios, including effective medium and geometric optics regimes, were studied.¹⁸ For each of these cases, texturing is performed outside of the active light-absorbing region of the solar cell.

Another effect of surface texturing is the trapping of certain light rays by total internal reflection. For a random

surface texture, leading to Lambertian probability distribution of deflected light rays, the effective path length of light within the absorbing medium is enhanced by a factor of $4n^2$, where n is refractive index of the medium.^{19,20} This leads to the so called Lambertian light trapping limit, an important benchmark for solar light trapping that has proved difficult to surpass in most solar cell designs. However, by texturing the interior, active regions of the solar cell, this Lambertian limit can be surpassed. Recently, it was shown that photonic crystal (PC) light trapping in a wave optics regime enables exceptional solar absorption in thin films.^{21–28} Most strikingly, it was shown that for slanted conical pore photonic crystals, it is possible to surpass the longstanding $4n^2$ Lambertian limit even after the absorption spectrum is integrated over the range of 400–1100 nm.²⁸ With a single micron of silicon (equivalent bulk thickness), this solar absorption corresponds to a maximum achievable photocurrent density (MAPD) of nearly $35\ \text{mA/cm}^2$. In more traditional solar cell architectures, such a large MAPD would require more than $100\ \mu\text{m}$ of silicon.

Silicon nanowire architectures offer an alternative type of thin film solar cell. There are many reports of design principles to minimize reflection and efficiently absorb sunlight in nanowires.^{29–34} Optimized solar absorption (for a fixed volume of silicon) can be obtained by arrangement of the nanowires into a photonic crystal with appropriate lattice constant and wire diameter. Additional modulation of the nanowire diameter along the vertical axis provides graded-index antireflection effects at the top of the array, light trapping in the middle section, and Bragg reflection near the bottom of the wires.³⁵ As in the case of conical nanopore photonic crystal, part of the light trapping occurs as a result of parallel-to-interface refraction (PIR) effects into slow group velocity modes.³⁶ While the optimized MAPD for nanowires is less than that of a conical pore photonic crystal, the nanowire provides opportunities for more efficient charge carrier collection.

Nanostructuring of the solar cell gives opportunities for nontrivial choice of pn-junction architecture and contact

^{a)}Electronic mail: deinega@physics.utoronto.ca

positioning. For example, a radial junction geometry in nanowires can be exploited to increase power conversion efficiency with poor quality silicon due to decoupling of light absorption and carrier collection directions.^{37–44} To calculate efficiency for nanostructured cells, optical and electrical modeling must be combined. The solution of Maxwell's equations provides the absorption profile inside the structure that defines the charge carrier generation profile. This profile is used as the input for the semiconductor drift-diffusion equations to calculate solar cell efficiency, including bulk and surface recombination losses.^{45–52}

In this paper, we present results for coupled optical and electrical modeling for nanopore photonic crystal solar cells. As a reference case, we also discuss a simple nanowire geometry. We consider photonic crystals with straight and slanted conical nanopores. We study the influence of recombination losses on the efficiency of the solar cell and identify optimal junction and contact geometries. We show that power conversion efficiency of 17.5% can be achieved in a slanted conical pore photonic crystal solar cells using only 1 μm of equivalent bulk thickness of silicon and significant contact recombination losses.

The rest of the paper is organized as follows. In Sec. II, we compare results for solar absorption distribution and carrier generation profile inside different nanostructured cells. In Sec. III, we calculate how the current and voltage of the solar cell vary with position of the p-n interface and contacts for various choice of the carrier diffusion lengths. Conclusions are given in Sec. IV.

II. SOLAR ABSORPTION MODELING

We first compare absorption properties for nanowires and nanopore PC films (Fig. 1). The equivalent bulk thickness for all considered structures is 1 μm . The geometrical parameters for two specific architectures are chosen in order to achieve maximal solar absorption using given equivalent bulk thickness. These parameters were found as a result

of optimization procedure performed in our previous works.^{28,35}

1. We consider a nanopore PC film of height 1.6 μm containing a square array of conical holes with radius $r = 0.5 \mu\text{m}$, filled with silica (refractive index $n = 1.5$). The lattice constant of this PC is $a = 0.85 \mu\text{m}$. The tip of each cone touches the center of the square unit cell (straight cones) or center of its side (slanted cones). The bottom metal contact is modeled as a perfect electric conductor that reflects all sunlight that reaches it. The top contact is an indium tin oxide (ITO) net of the height 50 nm and width 150 nm (refractive index $n = 1.8$). The top of the solar cell is covered with partial silica hemispheres with height 0.2 μm above the silicon film and radius 0.5 μm .
2. We consider nanowires with the radius $r = 0.082 \mu\text{m}$ and height $h = 6.3 \mu\text{m}$, arranged in a square lattice photonic crystal with period $a = 0.35 \mu\text{m}$. The silicon nanowire PC is fully embedded in a silica slab (refractive index $n = 1.5$) of height equal to nanowires. The bottom metal contact is modelled as a perfect electric conductor. The top contact is an ITO film of thickness 50 nm, touching each nanowire.

We note that the nanowires surface shape can be separately optimized to provide considerable improvement in MAPD. In previous work,³⁵ we showed that by appropriate modulation of the nanowire surface, light trapping enhancement occurs by parallel-to-interface refraction into slow light modes. For our present comparative purposes, we consider only straight cylindrical nanowires.

We calculate solar absorption using the finite-difference time-domain (FDTD) method⁵³ with the help of the *Electromagnetic Template Library*.⁵⁴ We assume that the entire solar spectrum is collimated into a normal angle of incidence. (Oblique incidence case can be simulated with the help of our FDTD iterative technique.^{55,56}) We use the standard FDTD scheme, where a plane wave impulse is directed onto the structure, fields are recorded, transformed to the

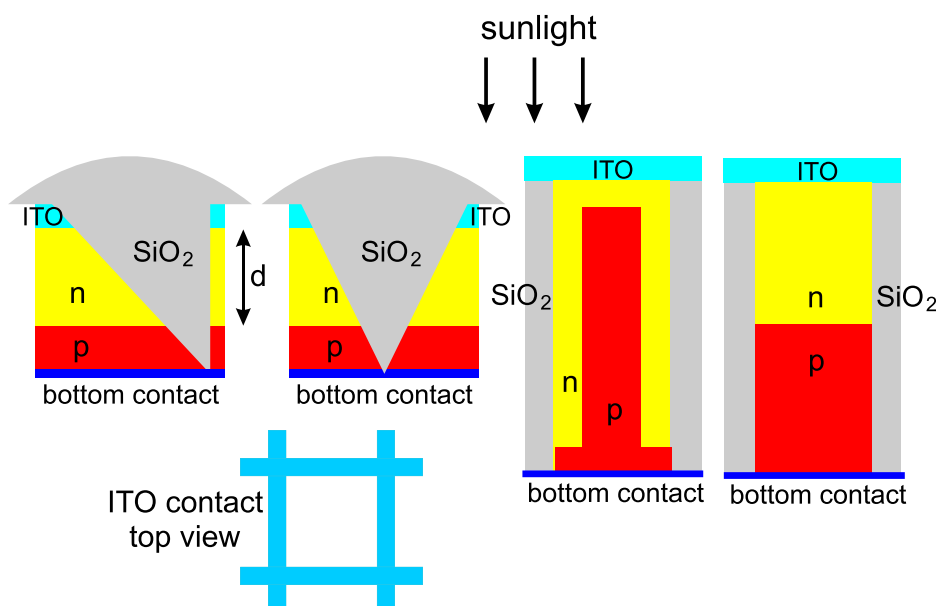


FIG. 1. From left to right, side view of (i) slanted conical pore PC film, (ii) straight conical pore PC film, (iii) nanowire with radial p-n junction, and (iv) nanowire with axial p-n junction. Lower left figure depicts top view of ITO top contact in conical pore PC geometry. Different scale is used for vertical and horizontal dimensions.

frequency domain, and normalized to the incident spectrum, to calculate the frequency dependent absorption at each point \mathbf{r} inside the structure

$$\alpha(\omega, \mathbf{r}) = \frac{\omega \cdot \text{Im}(\varepsilon) |\mathbf{E}(\omega, \mathbf{r})|^2}{c \cdot \text{Re}[\mathbf{E}_{\text{inc}}(\omega, \mathbf{r}), \mathbf{H}_{\text{inc}}^*(\omega, \mathbf{r})]}. \quad (1)$$

Here, c is the speed of light in vacuum, ω is the frequency of light and ε is silicon dielectric function. For nanowire and straight conical pore PC, we model linear light polarization along one periodic direction. For the slanted conical pore PC, we perform two numerical experiments for linear polarization along the two distinguishable periodic directions, and then average the results.

We use a subpixel smoothing technique⁵⁷ to eliminate any staircase effect caused by our rectangular FDTD mesh. This technique has been shown to significantly improve the accuracy of the FDTD calculations for arbitrary shaped scatterers. For reducing numerical reflection from the artificial absorbing perfectly matched layer (PML),⁵³ we use additional back absorbing layers technique.⁵⁸

Experimental data on the silicon dielectric permittivity $\varepsilon(\omega)$ are taken from Ref. 59. The frequency dependence of $\varepsilon(\omega)$ is assigned in FDTD by considering a modified Lorentz approximation where the dielectric polarization depends both on the electric field and its first time derivative⁶⁰

$$\varepsilon(\omega) = \varepsilon_\infty + \sum_{p=1}^2 \frac{\Delta\varepsilon(\omega_p^2 - i\gamma'_p\omega)}{\omega_p^2 - 2i\omega\gamma_p - \omega^2}, \quad (2)$$

with $(\omega_p, \gamma_p, \text{ and } \gamma'_p)$ in units of $(\mu\text{m})^{-1}$, and the speed of light is unity): $\varepsilon_\infty = 1, \Delta\varepsilon_1 = 8.93, \Delta\varepsilon_2 = 1.855, \omega_1 = 3.42$ (corresponding to wavelength $\lambda_1 \approx 0.292\mu\text{m}$), $\omega_2 = 2.72$ ($\lambda_2 \approx 0.368\mu\text{m}$), $\gamma_1 = 0.425, \gamma_2 = 0.123, \gamma'_1 = 0.087, \gamma'_2 = 2.678$. This model provides an accurate fit to the response of bulk crystalline silicon to sunlight over the wavelength range from 300 to 1000 nm, while conventional Debye, Drude, and Lorentz approximations fail. Fitting of the silicon dielectric function is found with the help of an open MATLAB script.⁶¹ The modified Lorentz approximation is implemented in FDTD using the auxiliary differential equation (ADE) technique.⁶⁰

We assume that each absorbed photon of energy larger than the silicon electronic bandgap leads to generation of an electron-hole pair. The electrons and holes are assumed to rapidly lose energy by scattering from phonons and occupy energy levels near the conduction and valence band edges, respectively. Subsequently the electron and hole dynamics is described by the drift-diffusion model.^{62,63} The total charge carrier generation rate per unit volume is obtained by integration of the calculated absorption $\alpha(\lambda, \mathbf{r})$ with incident solar Air Mass 1.5 Global Spectrum⁶⁴ intensity $I(\lambda)$, in units of energy per unit area per unit time, per unit wavelength, over the wavelength range of 350–1000 nm

$$G(\mathbf{r}) = \int_{\lambda_{\text{min}}}^{\lambda_{\text{max}}} \frac{\lambda}{hc} I(\lambda) \alpha(\lambda, \mathbf{r}) d\lambda. \quad (3)$$

Here, the photon energy is $\frac{hc}{\lambda}$, wavelength $\lambda = \frac{2\pi c}{\omega}$, and h is Planck's constant.

The MAPD, in which all generated carriers are assumed to be collected, is calculated by integrating the generation rate (3) over the photonic crystal unit cell volume V_s and dividing by the surface area a^2 of the unit cell

$$\text{MAPD} = \frac{1}{a^2} \int_{V_s} eG(\mathbf{r}) d\mathbf{r}. \quad (4)$$

Here, a is the PC lattice constant and e is electron charge. The case of 100% solar absorption over the 350–1000 nm range in crystalline silicon corresponds to $\text{MAPD} = 42.3 \text{ mA/cm}^2$.

In Fig. 2, we present the calculated absorption profile $\alpha(\lambda, r, z)$ for the slanted conical pore PC film. Calculated MAPD for our slanted conical pore PC film with silica packaging is 33.3 mA/cm^2 . For the straight conical pore PC film, this drops to 30.4 mA/cm^2 , and for our cylindrical nanowires, the MAPD is 20.7 mA/cm^2 . As shown in previously,³⁵ by appropriate modulation of the nanowire surface the latter MAPD can improved up to 27.7 mA/cm^2 .

III. JUNCTION GEOMETRY OPTIMIZATION

To model electrical transport, we simultaneously solve the Poisson equation and continuity equations for electrons and holes

$$\nabla^2 \psi = -\frac{q}{\varepsilon} (p - n + N_D - N_A), \quad (5)$$

$$\nabla J_n = -\nabla J_p = q(R - G), \quad (6)$$

$$J_n = qD_n \nabla n - q\mu_n n \nabla \psi, \quad (7)$$

$$J_p = -qD_p \nabla p - q\mu_p p \nabla \psi, \quad (8)$$

where ψ is the electrostatic potential, q is the elementary electronic charge, ε is the dielectric function, n and p are electron and hole densities, N_D and N_A are concentrations of ionized donors and acceptors, R and G are recombination

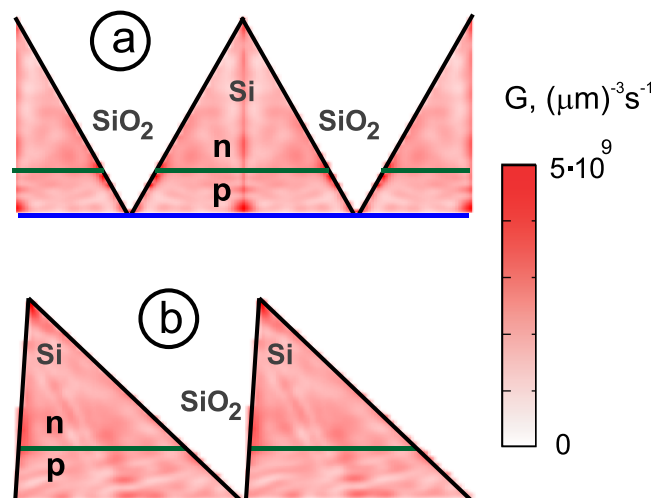


FIG. 2. Total charge carrier generation rate profile (see Eq. (3)) inside (a) straight and (b) slanted conical pore PC film. Different scale for vertical and horizontal dimensions is used.

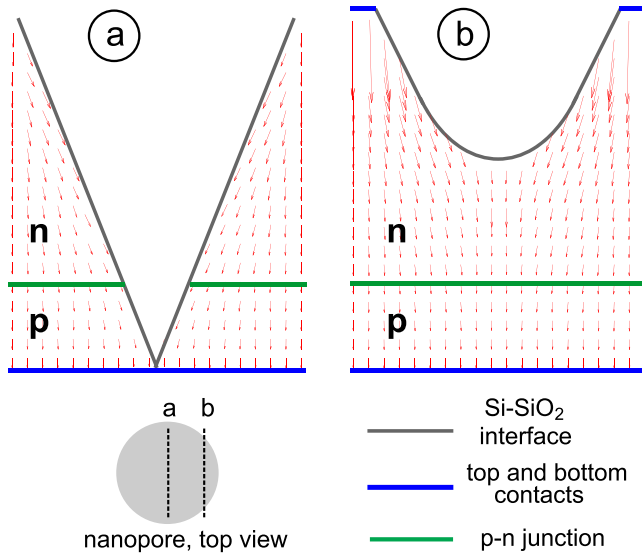


FIG. 3. Photocurrent density distribution inside (a) central slice and (b) side slice in the straight conical pore PC film. Different scale for vertical and horizontal dimensions is used.

and generation rates, J_i , D_i , and μ_i are current densities, diffusion coefficients, and mobilities, $i = n, p$.

The generation rate profile, calculated using Eqs. (1) and (3), is used as an input to the continuity equation (6). All transport calculations are performed using our 3D semiconductor device modeling library *Microvolt*.⁶⁵ Nanowire modeling is simplified using an angular average of the generation profile. This is a good approximation which reduces dimensionality of the problem from 3D (x, y, z) to 2D (r, z). This is solved using a simple radial finite difference scheme.⁴⁵

In our calculations, we use silicon parameters found in Ref. 37:

- (i) doping concentration $N_d = N_a = 10^{18} \text{ cm}^{-3}$,
- (ii) electron and hole mobilities $\mu_n = 270 \text{ cm}^2 \text{ V}^{-1} \text{ s}^{-1}$ and $\mu_p = 95 \text{ cm}^2 \text{ V}^{-1} \text{ s}^{-1}$, respectively. The diffusion coefficients D_n and D_p are then calculated using the Einstein relation $D = \frac{kT}{e} \mu$ (temperature T is assumed to be 300 K throughout the solar cell).

As in earlier literature,^{37,46} we consider only Shockley-Reed-Hall (SRH) recombination from a single-trap level that lies near the middle of the bandgap

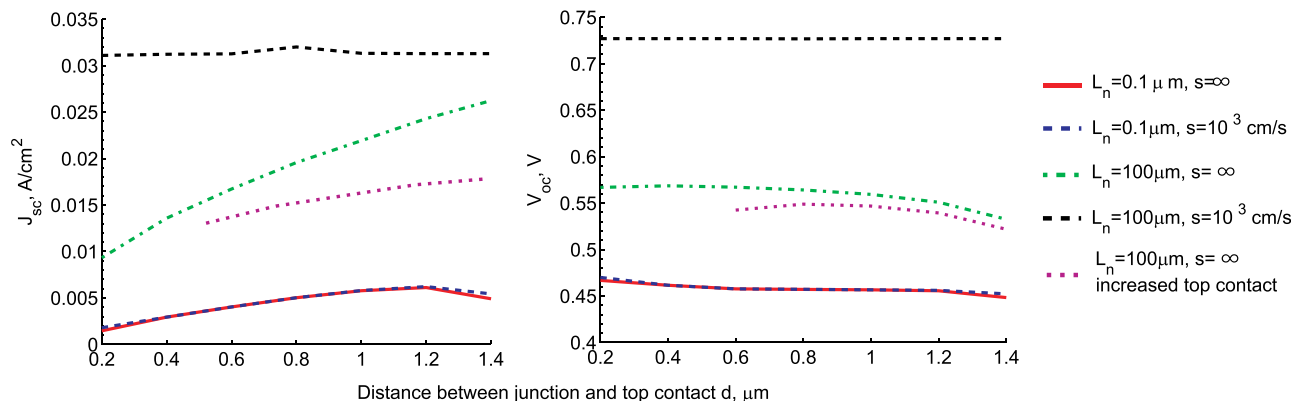


FIG. 4. Short circuit current density J_{sc} and open circuit voltage V_{oc} as a function of distance between junction and top surface of the slanted conical pore PC film for various diffusion lengths L_n and surface recombination at the contacts s values. All geometrical parameters are listed at the beginning of Sec. II.

$$R = \frac{np - n_i^2}{\tau_p(n + n_i) + \tau_n(p + n_i)}. \quad (9)$$

Here, n_i is intrinsic charge carrier concentration. We choose the lifetime of the minority electrons in the p-region equal to the lifetime of minority holes in the n-region $\tau_n = \tau_p$. In the following, we consider the diffusion length $L_n = \sqrt{\tau_n D_n}$ as an independent variable. Including Auger and radiative recombination¹ in our model for R results primarily in a change of the diffusion length L_n . Rather than adding these other recombination channels into the microscopic expression (9), for simplicity we subsume these processes as done previously⁴⁶ into the overall diffusion length L_n .

We impose a surface recombination velocity of 100 cm s^{-1} at each Si-SiO₂ interface, consistent with available experimental data.^{2,40} As shown previously,⁴⁶ increasing the surface recombination velocity at the Si-SiO₂ interface from 100 cm s^{-1} to 1000 cm s^{-1} leads to only slight (1%–2%) reduction of short-circuit current density and open-circuit voltage. Contacts are assumed to be ohmic with a larger surface recombination velocity s which we vary in the range $10^3 \text{ cm s}^{-1} \leq s \leq \infty$. We model the p-n junction and contact geometries as in Fig. 1. For our conical pore PC, the junction interface is parallel to the bottom surface. For nanowires we consider both radial and axial junction geometries.

For illustration, we present typical photocurrent distributions inside the straight conical pore PC film in Fig. 3. The short circuit current density J_{sc} is calculated as the current flux through the contact (bottom or top) area inside the square lattice unit cell normalized to this unit cell area a^2 ($a = 750 \text{ nm}$ for conical pore PC film and $a = 350 \text{ nm}$ for nanowire PC).

We calculate the short circuit current density J_{sc} and open circuit voltage V_{oc} for different values of L_n and s , varying the distance d between the p-n junction and top surface of the PC film (Fig. 4). If the diffusion length is smaller than film width ($L_n = 0.1 \mu\text{m}$ in Fig. 4), the results are almost independent of surface recombination. In this case, only carriers that are close to the p-n junction contribute to the photocurrent. These carriers are quickly separated across the junction and have minimal subsequent opportunity to recombine. Other carriers recombine mostly in the bulk, not at the surface. Therefore, the optimal junction position is located in

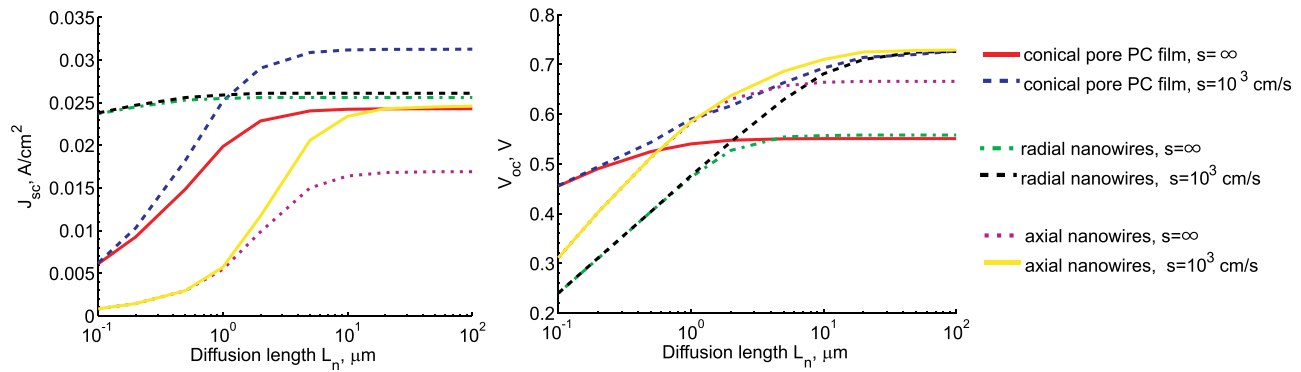


FIG. 5. Short circuit current density J_{sc} and open circuit voltage V_{oc} for slanted conical pore PC film, radial, and axial nanowires as a function of diffusion length L_n for various contact surface recombination velocities s . All geometrical parameters are listed at the beginning of Sec. II.

the region where most of the light is absorbed and most carriers are generated. The highest absorption rate is at the top surface of PC film, however, the highest filling fraction of silicon is at the bottom surface. The competition between these two factors determines the optimal junction position at $d = 1.2 \mu\text{m}$ below the top surface (see maximum of blue and red curves in Fig. 4, left). If the carrier diffusion length is longer than the film depth ($L_n = 100 \mu\text{m}$ in Fig. 4) and surface recombination is high ($s = \infty$ in Fig. 4), generated carriers are most likely to recombine at the contacts. Since the surface area of the bottom contact is larger than the surface area of the top one, photocurrent improves when the junction position shifts to the bottom contact. This enables carriers generated near the bottom of the photonic crystal to “escape” from the bottom contact and be separated by the junction (green curve in Fig. 4, left). However, as we increase the top contact area, the improvement is less pronounced. To illustrate this, we consider a situation where the top contact extends to the surface of the conical hole $z \geq 0.9 \mu\text{m}$, where the coordinate z increases from 0 (bottom of the film) to $1.6 \mu\text{m}$ (top of the film), see Fig. 6(i). For this geometry, we use the charge carrier generation profile obtained for the geometry in Fig. 1(i), in order to isolate the recombination influence of the extended contact from possible absorption profile changes. Results are represented by the magenta curve in Fig. 4, left. If the recombination losses are negligible ($L_n = 100 \mu\text{m}$ and $s = 10^3 \text{ cm/s}$), then J_{sc} and V_{oc} are almost independent of junction position. In this case, J_{sc} is approximately equal to the MAPD (black curve in Fig. 4), since nearly all generated carriers contribute to the photocurrent.

The open circuit voltage V_{oc} depends only weakly on junction position d , but in the opposite way: V_{oc} slightly improves if the junction shifts closer to the top surface (Fig. 4, right). In this case, the junction area becomes smaller (Fig. 1) resulting in reduced recombination of excess carriers in the depletion region. As discussed below, this improves V_{oc} .

In Fig. 5, we compare J_{sc} and V_{oc} for slanted conical pore PC films and nanowires with radial and axial junction geometries. Results are given as a function of diffusion lengths L_n for small ($s = 10^3 \text{ cm/s}$) and high ($s = \infty$) surface recombination rates at the contacts. The distance between the p-n junction and top surface of the conical pore PC film

is chosen to be $d = 1.2 \mu\text{m}$. This is close to the optimal value for small diffusion lengths (see maximum of blue and red curves in Fig. 4, left). The radial junction of the nanowire consists of two parts (Fig. 1): horizontal surfaces $0.1 \mu\text{m}$ from the top and bottom contacts and vertical surface $0.05 \mu\text{m}$ from the nanowire surface. Our axial junction model separates the nanowire into two layers of equal height.

For small L_n , J_{sc} , and V_{oc} are independent of surface recombination, since most of the recombination occurs in the bulk. In this case, only carriers generated close enough to the junction contribute to the photocurrent. Carriers generated further than L_n from the junction are highly susceptible to bulk recombination. In other words, the effective volume of silicon producing photocurrent is the volume within the distance L_n to the junction. The radial junction provides the highest value of J_{sc} for small carrier diffusion lengths, since it has the most developed junction area with largest catchment volume for separating newly generated carriers. Nanowires with axial junction provide the smallest J_{sc} since the effective volume of silicon providing photocurrent is a small fraction of the whole nanowire volume.

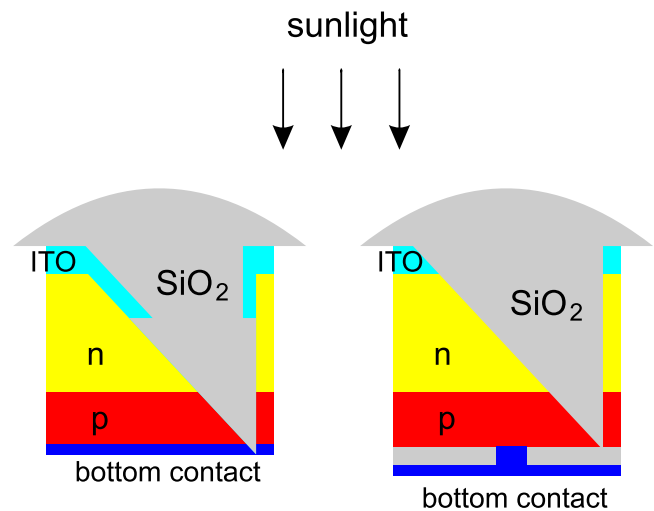


FIG. 6. (i) Slanted conical pore PC film with extended top contact and planar bottom contact, (ii) slanted conical pore PC film with reduced top contact (see Fig. 1) and bottom contact consisting of square lattice of protruding dots and intervening SiO_2 layer. Different scale for vertical and horizontal dimensions is used.

If the diffusion length L_n and the surface recombination velocity s are large, most of the recombination occurs at the metal contacts. The radial junction yields the largest J_{sc} since carriers are more likely to “escape” contact recombination and reach the junction where they become separated. For long diffusion lengths L_n and small surface recombination velocity s (no recombination losses), J_{sc} approaches the MAPD for each of the structures. The conical pore PC produces the highest J_{sc} , since it has highest MAPD.

The radial junction nanowire produces the smallest open circuit voltage V_{oc} of all architectures considered. This is due to the negative influence of excess carrier recombination in the depletion region.¹ When these carriers recombine, additional carriers diffuse to the depletion region to make up for this loss. This diffusive flow of carriers constitutes a recombination current that is opposite to the required photocurrent drift. The backflow recombination current is greater if the depletion (and junction) region is more developed. Therefore, a more developed junction area produces a smaller open circuit voltage V_{oc} . This explains the smaller values of V_{oc} for the radial junction nanowire geometry. Using silicon of high quality in the depletion region around the junction can improve V_{oc} , even if the silicon quality elsewhere is small.⁴⁶

For the axial nanowire geometry, the volume of silicon within a diffusion length of the junction is much smaller than the total silicon volume. In the case of small diffusion length, axial nanowires produce smaller V_{oc} than the conical pore PC film. This is explained by the smaller photocurrent J_{sc} for axial nanowires. For each value of applied voltage, the total current is a sum of the photocurrent and the forward bias current,¹ which is opposite to the photocurrent. Forward bias current is caused by diffusion of carriers to the region with opposite doping, which increases with applied voltage.¹ In the case of smaller photocurrent J_{sc} , a correspondingly smaller voltage V_{oc} is required to produce forward bias current with magnitude equal to the photocurrent, so the total open circuit current is zero.

For long diffusion lengths L_n and small surface recombination velocity s (no recombination losses), all structures exhibit a similar V_{oc} value ~ 0.73 V.

We now compare the power conversion efficiency of straight and slanted conical pore PC films, nanowires with axial and radial junctions, and a planar silicon solar cell of thickness $1 \mu\text{m}$. The geometrical parameters in all cases are chosen to use the same amount of silicon as in the planar cell. The surface recombination velocity at the contacts is chosen to be 10^5 cm s^{-1} , as in Refs. 37 and 46.

For a conical pore PC film geometry with diffusion length exceeding the film thickness, carriers recombine mostly at the contact surface (compare red and blue curves in Fig. 5). The influence of contact recombination can be suppressed by reducing the semiconductor-metal interface area and passivating the remaining rear surface with silica. This has been demonstrated for wafer-based silicon solar cells using a square array of dot shaped rear contacts of the radius $r = 10 \mu\text{m}$, spaced by $a = 200 \mu\text{m}$ from each other.¹ The back contact area fraction for this geometry $\pi r^2/a^2$ is then less than 1% of the total back-surface area. In our model we simulate reduced

rear contact surface area using a periodic array of cylindrical dots of radius 50 nm and height 50 nm , corresponding to a contact area $\sim 1\%$ of the total back-surface area, see Fig. 6(ii). We also use a highly doped region ($N_a = 5 \times 10^{18} \text{ cm}^{-3}$) with thickness 50 nm near rear contact (back surface field). The interface between the higher and lower doped regions behaves like a p-n junction where the resulting electric field makes a potential barrier to minority carrier flow to the surface.¹ As a result, these carriers are more likely to cross the p-n junction into the region with opposite doping and contribute to the photocurrent. On the other hand, the interface between higher and lower doped regions enhances the flow of majority carriers in the direction of the photocurrent.

We obtain the generation rates for conical pore PC and nanowires from our FDTD simulations of Maxwell’s equations. The generation rate for the planar cell is estimated using Beer’s law for absorption and assuming no reflection from the front (perfect antireflective coating) and back sides of the cell, as in Ref. 37. The calculated efficiencies as a function of diffusion length are plotted in Fig. 7. Results for the planar cell are in excellent agreement with analytical results.³⁷ The photonic crystal solar cells exhibit higher efficiency than the planar cell due to light-trapping and enhanced absorption. The radial junction shows the best efficiency for very small diffusion lengths due to the more developed junction area. For medium to long diffusion lengths, the best efficiency of 17.5% is demonstrated by the slanted conical pore PC film due to its higher solar absorption. This is comparable with the best efficiency of commercial planar silicon solar modules with the cell thickness more than $100 \mu\text{m}$.¹⁻³

As in the case of conventional solar cells, a smaller doping concentration N increases the saturation current J_0 (leakage of thermally generated minority carriers across the junction) that, in turn, leads to smaller open-circuit voltage

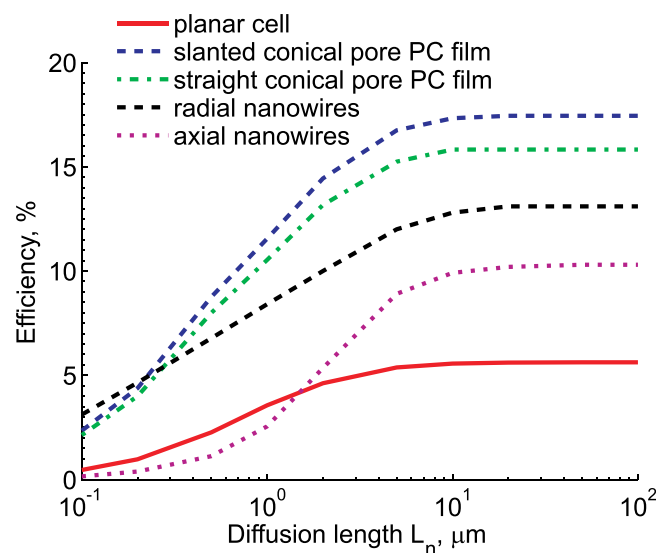


FIG. 7. Power conversion efficiency as a function of diffusion length L_n for different cells with the same volume of silicon, equivalent to the volume of a planar cell of $1 \mu\text{m}$ thickness. All geometrical parameters are listed at the beginning of Sec. II. For the planar cell, a perfect antireflection coating is assumed. Surface recombination velocity at the contact s is chosen to be 10^5 cm s^{-1} .

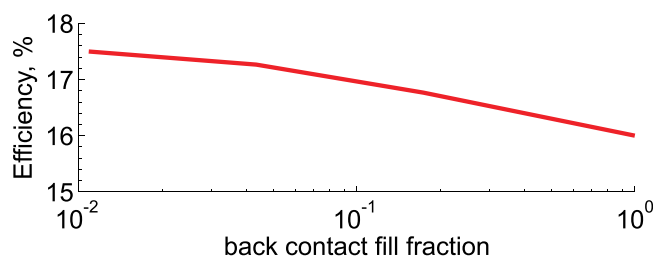


FIG. 8. Power conversion efficiency as a function of back contact filling fraction for the slanted conical pore PC film. Diffusion length $L_n = 10 \mu\text{m}$ and surface recombination velocity at the contact s is 10^5 cm s^{-1} .

and lower efficiency.¹ By lowering the doping concentration in our slanted conical pore PC from 10^{18} cm^{-3} to 10^{17} cm^{-3} and 10^{16} cm^{-3} , the efficiency drops from 17.5% to 15.6% and 13.7% correspondingly. In the limit of zero doping, there is no electric field in the junction area to provide photocurrent and power conversion efficiency goes to zero.

As discussed above, reducing the back contact area leads to improved efficiency. The rate of improvement is highest for a back contact fill fraction of 100%, corresponding to a flat contact (Fig. 8). For our choice of back contact (cylindrical dots of the radius 50 nm) the rate of further improvement is very small. In other words, further reduction of the contact area does not lead to significant efficiency improvement.

IV. DISCUSSION

Our calculated power conversion efficiency of 17.5% for a $1 \mu\text{m}$ (equivalent bulk thickness) slanted conical pore silicon PC solar cell provides only a baseline result. The efficiency can be improved in various ways. A simple improvement is achieved using amorphous and microcrystalline silicon in the top and bottom regions, respectively, to form a tandem solar cell. Both forms of silicon can be manufactured using the same technology.¹ Such tandem cells have been studied previously for planar⁶⁶ and nanowire^{67,68} geometries. Amorphous silicon and crystalline silicon have bandgaps well suited for tandem cells (1.7 eV and 1.12 eV, respectively). The absorption coefficient of amorphous silicon is about an order of magnitude greater than in crystalline silicon at visible wavelengths. However, amorphous silicon has poor transport properties with a short carrier diffusion length and carriers photogenerated in p or n layers are unlikely to contribute to the photocurrent. To overcome this problem, a p-i-n junction with undoped or intrinsic region is used.¹ The built-in bias is dropped across the undoped region, creating an electric field there. Carriers photogenerated in the undoped region are driven by this electric field to produce a photocurrent.

Our initial crystalline silicon slanted conical pore PC film already absorbs 95% of sunlight with energy higher than the electronic bandgap of amorphous silicon. Therefore, using amorphous silicon at the top does not increase the overall amount of absorbed sunlight. It simply redistributes the carrier generation profile along the depth of conical pore PC film. The thickness of the amorphous silicon

segment is ideally chosen such that the same amount of photocurrent is produced in the amorphous and crystalline silicon layers. Employing separate p-i-n and p-n junctions for each segment yields two solar cells connected in series. Adjacent n-doped and p-doped regions of these subcells can be heavily doped to form a tunnel junction between the subcells. Current passes through the tunnel junction between the subcells by quantum tunneling.¹ The photocurrent in the resulting tandem cell is equal to the photocurrent in each subcell, while the total voltage is a sum of subcell voltages. For a crystalline silicon subcell, we expect $V_{oc} = 0.6\text{V}$, whereas for the amorphous silicon subcell, we expect $V_{oc} = 0.9\text{V}$ according to recent experimental^{69,70} and numerical⁷¹ results. Therefore, the total open circuit voltage is 1.5 V. Photocurrent in the tandem cell is one half that of the initial silicon conical PC film cell, since the same amount of sunlight is absorbed by the two subcells. Therefore, we obtain around 25% improvement in efficiency relative to the initial silicon conical pore PC film. This suggests a tandem cell with 21.9% power conversion efficiency.

Improvement in the contact regions can also provide substantial gain in power conversion efficiency. For diffusion lengths longer than the thickness of the conical pore PC film, photogenerated carriers recombine mostly at the contacts. As we found numerically, if the surface recombination velocity at the contacts is lowered until 100 cm s^{-1} , the efficiency improves from 17.5% to 22.5% when diffusion length L_n is equal to $10 \mu\text{m}$. Similarly, for the tandem solar cell we expect efficiency improvement from 21.9% to 25.5%. The possibility of achieving small surface recombination velocity at the contacts by passivation with an intrinsic amorphous buffer layer has recently been presented.⁷²

We note finally that the buffer region of SiO_2 between the structured metallic back contact (Fig. 6(ii)) and the light-absorbing silicon photonic crystal may be replaced with material that up-converts photons in the 1100–1500 nm wavelength range to photons of energy higher than the silicon band gap. Nearly 19% of incoming solar power is lost due to photons below the silicon band gap that cannot otherwise be absorbed. Dye-sensitized, erbium nano-particles may provide a key to such broadband up-conversion.⁷³ A significant feature of the conical pore PC film is that it provides not only light-trapping but also strong light concentration in specific regions with intensity enhancement of about 100 times the average intensity.²⁸ A suitably structured metallic back-contact can provide further intensity enhancement through plasmonic resonances. The resulting strong solar concentration effects can facilitate nonlinear up-conversion of sub-bandgap light. If in this way solar power conversion efficiency could reach 30% or more with only $1 \mu\text{m}$ of silicon, it would be a major advance in solar cell technology.

ACKNOWLEDGMENTS

This work was supported in part by the United States Department of Energy Contract No. DE-FG02-10ER46754, the Natural Sciences and Engineering Research Council of Canada, and the Canadian Institute for Advanced Research.

- ¹J. Nelson, *The Physics of Solar Cells* (Imperial College Press, London, 2003).
- ²M. Green, *Silicon Solar Cells: Advanced Principles and Practice* (Centre for Photovoltaic Devices and Systems, Sydney, 1995).
- ³M. Green, *Third Generation Photovoltaics* (Springer, Berlin, 2006).
- ⁴*Nanotechnology for Photovoltaics*, edited by L. Tsakalacos (CRC Press, 2010).
- ⁵G. Beaucarne, "Silicon thin-film solar cells," *Adv. OptoElectron.* **2007**, 36970 (2007).
- ⁶C. G. Bernhard, "Structural and functional adaptation in a visual system," *Endeavour* **26**, 79–84 (1967).
- ⁷P. B. Clapham and M. C. Hutley, "Reduction of lens reflexion by the 'Moth Eye' principle," *Nature* **244**, 281–282 (1973).
- ⁸W. Southwell, "Gradient-index antireflection coatings," *Opt. Lett.* **8**, 584–586 (1983).
- ⁹C.-H. Sun, P. Jiang, and B. Jiang, "Broadband moth-eye antireflection coatings on silicon," *Appl. Phys. Lett.* **92**, 061112 (2008).
- ¹⁰C.-H. Chang, J. Dominguez-Caballero, H. Choi, and G. Barbastathis, "Nanostructured gradient-index antireflection diffractive optics," *Opt. Lett.* **36**, 2354–2356 (2011).
- ¹¹Q. Yang, X. A. Zhang, A. Bagal, W. Guo, and C.-H. Chang, "Antireflection effects at nanostructured material interfaces and the suppression of thin-film interference," *Nanotechnology* **24**, 235202 (2013).
- ¹²O. Bucci and G. Franceschetti, "Scattering from wedge-tapered absorbers," *IEEE Trans. Antennas Propag.* **19**, 96–104 (1971).
- ¹³B. L. Soporì and R. A. Pryor, "Design of antireflection coatings for textured silicon solar cells," *Sol. Cells* **8**, 249–261 (1983).
- ¹⁴Y. Kanamori, M. Sasaki, and K. Hane, "Broadband antireflection gratings fabricated upon silicon substrates," *Opt. Lett.* **24**, 1422–1424 (1999).
- ¹⁵S. A. Boden and D. M. Bagnall, "Tunable reflection minima of nanostructured antireflective surfaces," *Appl. Phys. Lett.* **93**, 133108 (2008).
- ¹⁶D. Poxson, M. Schubert, F. Mont, E. Schubert, and J. K. Kim, "Broadband omnidirectional antireflection coatings optimized by genetic algorithm," *Opt. Lett.* **34**, 728–730 (2009).
- ¹⁷B. Paivanranta, T. Saastamoinen, and M. Kuittinen, "A wide-angle antireflection surface for the visible spectrum," *Nanotechnology* **20**, 375301 (2009).
- ¹⁸A. Deinega, I. Valuev, B. Potapkin, and Yu. Lozovik, "Minimizing light reflection from dielectric textured surfaces," *J. Opt. Soc. Am. A* **28**(5), 770–777 (2011).
- ¹⁹E. Yablonovitch, "Statistical ray optics," *J. Opt. Soc. Am.* **72**, 899–907 (1982).
- ²⁰P. Campbell and M. A. Green, "Light trapping properties of pyramidally textured surfaces," *J. Appl. Phys.* **62**, 243–249 (1987).
- ²¹P. Bermel, C. Luo, L. Zeng, L. C. Kimerling, and J. D. Joannopoulos, "Improving thin-film crystalline silicon solar cell efficiencies with photonic crystals," *Opt. Express* **15**, 16986–17000 (2007).
- ²²D. Zhou and R. Biswas, "Photonic crystal enhanced light-trapping in thin film solar cells," *J. Appl. Phys.* **103**, 093102 (2008).
- ²³R. Dewan and D. Knipp, "Light trapping in thin-film silicon solar cells with integrated diffraction grating," *J. Appl. Phys.* **106**, 074901 (2009).
- ²⁴Z. Yu, A. Raman, and S. Fan, "Fundamental limit of light trapping in grating structures," *Opt. Express* **18**, 366–380 (2010).
- ²⁵S. E. Han and G. Chen, "Toward the Lambertian limit of light trapping in thin nanostructured silicon solar cells," *Nano Lett.* **10**, 4692–4696 (2010).
- ²⁶S. B. Mallick, M. Agrawal, and P. Peumans, "Optimal light trapping in ultra-thin photonic crystal crystalline silicon solar cells," *Opt. Express* **18**, 5691–5706 (2010).
- ²⁷S. Sandhu, Z. Yu, and S. Fan, "Detailed balance analysis of nonphotonic solar cells," *Opt. Express* **21**, 1209–1217 (2013).
- ²⁸S. Eyderman, S. John, and A. Deinega, "Solar light trapping in slanted conical-pore photonic crystals: Beyond statistical ray trapping," *J. Appl. Phys.* **113**, 154315 (2013).
- ²⁹L. Hu and G. Chen, "Analysis of optical absorption in silicon nanowire arrays for photovoltaic applications," *Nano Lett.* **7**(11), 3249–3252 (2007).
- ³⁰J. S. Li, H. Y. Yu, S. M. Wong, X. C. Li, G. Zhang, P. G. Q. Lo, and D. L. Kwong, "Design guidelines of periodic Si nanowire arrays for solar cell application," *Appl. Phys. Lett.* **95**, 243113 (2009).
- ³¹C. Lin and M. L. Povinelli, "Optical absorption enhancement in silicon nanowire arrays with a large lattice constant for photovoltaic applications," *Opt. Express* **17**, 19371–19381 (2009).
- ³²V. Sivakov, G. Andra, A. Gawlik, A. Berger, J. Plentz, F. Falk, and S. H. Christiansen, "Silicon nanowire-based solar cells on glass: Synthesis, optical properties, and cell parameters," *Nano Lett.* **9**(4), 1549–1554 (2009).
- ³³E. Garnett and P. Yang, "Light trapping in silicon nanowire solar cells," *Nano Lett.* **10**, 1082–1087 (2010).
- ³⁴S. Han and G. Chen, "Optical absorption enhancement in silicon nanohole arrays for solar photovoltaics," *Nano Lett.* **10**, 1012–1015 (2010).
- ³⁵G. Demesy and S. John, "Solar energy trapping with modulated silicon nanowire photonic crystals," *J. Appl. Phys.* **112**, 074326 (2012).
- ³⁶A. Chutinan and S. John, "Light trapping and absorption optimization in certain thin-film photonic crystal architectures," *Phys. Rev. A* **78**, 023825 (2008).
- ³⁷B. M. Kayes, H. A. Atwater, and N. S. Lewis, "Comparison of the device physics principles of planar and radial p-n junction nanorod solar cells," *J. Appl. Phys.* **97**, 114302 (2005).
- ³⁸B. Z. Tian, X. L. Zheng, T. J. Kempa, Y. Fang, N. F. Yu, G. H. Yu, J. L. Huang, and C. M. Lieber, "Coaxial silicon nanowires as solar cells and nanoelectronic power sources," *Nature* **449**, 885 (2007).
- ³⁹L. Tsakalacos, J. Balch, J. Fronheiser, B. A. Korevaar, O. Sulima, and J. Rand, "Silicon nanowire solar cells," *Appl. Phys. Lett.* **91**, 233117 (2007).
- ⁴⁰M. D. Kelzenberg, D. B. Turner-Evans, B. M. Kayes, M. A. Filler, M. C. Putnam, N. S. Lewis, and H. A. Atwater, "Photovoltaic measurements in single-nanowire silicon solar cells," *Nano Lett.* **8**, 710 (2008).
- ⁴¹Z. Fan, H. Razavi, J. Do, A. Moriwaki, O. Ergen, Y.-L. Chueh, P. W. Leu, J. C. Ho, T. Takahashi, L. A. Reichertz, S. Neale, K. Yu, M. Wu, J. W. Ager, and A. Javey, "Three dimensional nanopillar array photovoltaics on low cost and flexible substrates," *Nature Mater.* **8**, 648 (2009).
- ⁴²H. Yoon, Y. Yuwen, C. Kendrick, G. Barber, N. Podraza, J. Redwing, T. Mallouk, C. Wronski, and T. Mayer, "Enhanced conversion efficiencies for pillar array solar cells fabricated from crystalline silicon with short minority carrier diffusion lengths," *Appl. Phys. Lett.* **96**, 213503 (2010).
- ⁴³K.-Q. Peng and S.-T. Lee, "Silicon nanowires for photovoltaic solar energy conversion," *Adv. Mater.* **23**, 198–215 (2011).
- ⁴⁴J. Christesen, X. Zhang, C. Pinion, T. Celano, C. Flynn, and J. Cahoon, "Design principles for photovoltaic devices based on Si nanowires with axial or radial p-n junctions," *Nano Lett.* **12**, 6024 (2012).
- ⁴⁵A. Deinega and S. John, "Finite difference discretization of semiconductor drift-diffusion equations for nanowire solar cells," *Comput. Phys. Commun.* **183**, 2128 (2012).
- ⁴⁶A. Deinega and S. John, "Solar power conversion efficiency in modulated silicon nanowire photonic crystals," *J. Appl. Phys.* **112**, 074327 (2012).
- ⁴⁷M. D. Kelzenberg, M. C. Putnam, D. B. Turner-Evans, N. S. Lewis, and H. A. Atwater, "Predicted efficiency of Si wire array solar cells," in Proceedings of the 34th IEEE PVSC (2009).
- ⁴⁸R. Kapadia, Z. Fan, and A. Javey, "Design constraints and guidelines for CdS/CdTe nanopillar based photovoltaics," *Appl. Phys. Lett.* **96**, 103116 (2010).
- ⁴⁹R. R. LaPierre, "Numerical model of current-voltage characteristics and efficiency of GaAs nanowire solar cells," *J. Appl. Phys.* **109**, 034311 (2011).
- ⁵⁰J. Foley, M. Price, J. Feldblyum, and S. Maldonado, "Analysis of the operation of thin nanowire photoelectrodes for solar energy conversion," *Energy Environ. Sci.* **5**, 5203–5220 (2012).
- ⁵¹M. Deceglie, V. Ferry, A. Alivisatos, and H. Atwater, "Design of nanostructured solar cells using coupled optical and electrical modeling," *Nano Lett.* **12**, 2894 (2012).
- ⁵²N. Huang, C. Lin, and M. L. Povinelli, "Limiting efficiencies of tandem solar cells consisting of III-V nanowire arrays on silicon," *J. Appl. Phys.* **112**, 064321 (2012).
- ⁵³A. Taflove and S. H. Hagness, *Computational Electrodynamics: The Finite Difference Time-Domain Method* (Artech House, Boston, 2005).
- ⁵⁴See <http://fdtd.kintechlab.com> for Electromagnetic Template Library (EMTL), Kintech Lab Ltd.
- ⁵⁵I. Valuev, A. Deinega, and S. Belousov, "Iterative technique for analysis of periodic structures at oblique incidence in the finite-difference time-domain method," *Opt. Lett.* **33**, 1491–1493 (2008).
- ⁵⁶I. Valuev, A. Deinega, and S. Belousov, "Implementation of the iterative finite-difference time-domain technique for simulation of periodic structures at oblique incidence," *Comput. Phys. Commun.* (unpublished).
- ⁵⁷A. Deinega and I. Valuev, "Subpixel smoothing for conductive and dispersive media in the FDTD method," *Opt. Lett.* **32**, 3429–3431 (2007).
- ⁵⁸A. Deinega and I. Valuev, "Long-time behavior of PML absorbing boundaries for layered periodic structures," *Comput. Phys. Commun.* **182**, 149–151 (2011).
- ⁵⁹M. A. Green and M. Keevers, "Optical properties of intrinsic silicon at 300 K," *Prog. Photovoltaics* **3**, 189–192 (1995).
- ⁶⁰A. Deinega and S. John, "Effective optical response of silicon to sunlight in the finite-difference time-domain method," *Opt. Lett.* **37**, 112–114 (2012).

- ⁶¹See <http://fdtd.kintechlab.com/en/fitting> for Program for fitting of dielectric function.
- ⁶²S. Selberherr, *Analysis and Simulation of Semiconductor Devices* (Springer, Wien, 1984).
- ⁶³R. Kircher and W. Bergner, *Three-Dimensional Simulation of Semiconductor Devices* (Birkhauser Verlag, 1991).
- ⁶⁴See <http://trredc.nrel.gov/solar/spectra/am1.5> for Air Mass 1.5 Global Spectrum.
- ⁶⁵See <https://sites.physics.utoronto.ca/sajeevjohn/software/microvolt> for Microvolt software for semiconductor devices modeling.
- ⁶⁶J. Meier, S. Dubail, S. Golay, U. Kroll, S. Fay, E. Vallat-Sauvain, L. Feitknecht, J. Dubail, and A. Shah, "Microcrystalline silicon and the impact on micromorph tandem solar cells," *Sol. Energy Mater. Sol. Cells* **74**, 457–467 (2002).
- ⁶⁷J. Zhu, Z. Yu, G. F. Burkard, C. M. Hsu, S. T. Connor, Y. Xu, Q. Wang, M. McGehee, S. Fan, and Y. Cui, "Optical absorption enhancement in amorphous silicon nanowire and nanocone arrays," *Nano Lett.* **9**, 279 (2009).
- ⁶⁸M. M. Adachi, M. P. Anantram, and K. S. Karim, "Optical properties of crystalline-amorphous core-shell silicon nanowires," *Nano Lett.* **10**, 4093–4098 (2010).
- ⁶⁹J. Kim, A. J. Hong, J.-W. Nah, B. Shin, F. M. Ross, and D. K. Sadana, "Three-dimensional a-Si:H solar cells on glass nanocone arrays patterned by self-assembled Sn nanospheres," *ACS Nano* **6**, 265 (2012).
- ⁷⁰C.-M. Hsu, C. Battaglia, C. Pahud, Z. Ruan, F.-J. Haug, S. Fan, C. Ballif, and Y. Cui, "High-efficiency amorphous silicon solar cell on a periodic nanocone back reflector," *Adv. Energy Mater.* **2**, 628 (2012).
- ⁷¹Z. Pei, S.-T. Chang, C.-W. Liu, and Y.-C. Chen, "Numerical simulation on the photovoltaic behavior of an amorphous-silicon nanowire-array solar cell," *IEEE Electron Device Lett.* **30**, 1305–1307 (2009).
- ⁷²P. J. Rostan, U. Rau, V. X. Nguyen, T. Kirchartz, M. B. Schubert, and J. H. Werner, "Low-temperature a-Si:H/ZnO/Al back contacts for high-efficiency silicon solar cell," *Sol. Energy Mater. Sol. Cells* **90**, 1345 (2006).
- ⁷³W. Zou, C. Visser, J. A. Maduro, M. S. Pshenichnikov, and J. C. Hummelen, "Broadband dye-sensitized upconversion of near-infrared light," *Nat. Photonics* **6**, 560–564 (2012).